How to cite: *Angew. Chem. Int. Ed.* **2025**, *64*, e202504652
doi.org/10.1002/anie.202504652

Organic Lasers

Peripheral Engineering of Multiple-Resonance Framework Targeting Efficient Organic Lasers

Tuul Tsagaantsooj, Xun Tang, Tao Zhang, Yi-Ting Lee, Rajat Walia, Xian-Kai Chen,* and Chihaya Adachi**

Abstract: Multiple-resonance thermally activated delayed fluorescent (MR-TADF) emitters have emerged as promising candidates for organic laser applications due to the potential for simultaneously achieving large oscillator strength and triplet utilization. In this study, we investigate the impact of peripheral *tert*-butyl (t-Bu)- and phenyl (Ph)-substituents on the typical 9-(phenylcarbazol-3-yl)-9H-carbazole-3-carbonitrile (CzBN) MR framework. Although these modifications preserve the frontier molecular orbital distribution with large oscillator strengths, they significantly influence excited-state dynamics and molecular aggregation even at low doping concentrations. Introducing Ph substituents extends the π–conjugation extension of CzBN, promoting closer molecular packing, detrimental molecular aggregation, and significantly broadening the excited-state absorption (ESA) band, which negatively impacts lasing performance. In contrast, CzBN-tBu, incorporating *t*-Bu groups as nonconjugated substituents, demonstrated reduced molecular aggregation and a distinct separation between the ESA band and stimulated emission region. Consequently, the optimal distributed feedback lasing performance is achieved by CzBN-tBu across various doping concentrations, resulting in the lowest lasing threshold of 3.4 μJ cm^{-2}. These findings underscore the impact of inherent aggregation at low doping ratios on lasing activities, highlighting the crucial role of rational peripheral engineering in modulating molecular interactions and excited-state dynamics, offering design strategies for developing MR lasing molecules.

Introduction

Laser technology, since its emergence in the 1960s, has revolutionized diverse fields, spurred by its unparalleled high-intensity, directionality, and coherence.[1] Within this landscape, organic lasers have garnered substantial interest, offering compelling advantages such as cost-effective fabrication, mechanical flexibility, and wavelength tunability.[2,3]

[*] T. Tsagaantsooj, X. Tang, Y.-T. Lee, C. Adachi
Center for Organic Photonics and Electronics Research (OPERA), Kyushu University, 744 Motooka, Nishi, Fukuoka 819-0395, Japan
E-mail: x-tang@opera.kyushu-u.ac.jp
adachi@opera.kyushu-u.ac.jp

T. Zhang, R. Walia, X.-K. Chen
Institute of Functional Nano & Soft Materials (FUNSOM), Soochow University, Suzhou, Jiangsu 215123, P.R. China
E-mail: xkchen@suda.edu.cn

C. Adachi
International Institute for Carbon-Neutral Energy Research (I2CNER), Kyushu University, 744 Motooka, Nishi, Fukuoka 819-0395, Japan

Additional supporting information can be found online in the Supporting Information section

The pursuit of high-performance organic solid-state lasers (OSSLs) has driven significant advances in both material design and device architecture.[3–7] A critical challenge, however, lies in achieving electrically pumped OSSLs, which necessitates efficient management of singlet and triplet excitons within a gain medium.[8–11] Conventional fluorescent gain materials predominantly utilize singlet excitons for stimulated emission, leaving triplet excitons unharnessed. This limitation leads to a high lasing threshold under long-pulsed photoexcitation and electrical pumping. Meanwhile, triplet accumulation can further induce energy losses through triplet-triplet annihilation (TTA), triplet-singlet annihilation, and excited-state absorption (ESA), hindering efficient light amplification.[12,13] Traditional strategies to mitigate triplet accumulation involve designing molecules with minimal overlap between their emission and triplet absorption bands or incorporating triplet scavengers and quencher hosts.[14–18] Therefore, rational manipulation of triplets is critical for optimal lasing performance. The thermally activated delayed fluorescence (TADF) technique has emerged as a promising pathway to circumvent the spin-forbidden transition of triplet excitons to the ground state by upconverting triplets to singlets via reverse intersystem crossing (RISC) in organic light-emitting diodes (OLEDs).[19,20] By enabling the utilization of both singlet and triplet excitons for lasing, TADF materials have the potential to reduce lasing thresholds and enhance device efficiency.[21–27]

Among TADF materials, multiple-resonance (MR) TADF emitters have recently attracted considerable attention due to their unique properties. Unlike conventional donor–acceptor

(D–A) type TADF molecules, MR-TADF emitters achieve a small singlet-triplet energy splitting (ΔE_{ST}) through the short-range MR interactions within a rigid and planar polycyclic aromatic framework.[28] This design strategy typically leads to narrow emission bandwidths, high photoluminescence quantum yields (PLQY), and enhanced molecular stability.[29] 5,9-Diphenyl-5,9-diaza-13b-boranaphtho[3,2,1-de]anthracene (DABNA)-based MR-TADF molecules have already demonstrated low amplified spontaneous emission (ASE) thresholds, making them promising candidates for realizing electrically driven OSSLs.[30,31] Recent advancements have focused on strategies to enhance RISC rates,[32–34] and improve the stability of MR-TADF emitters under high excitation densities.[35] However, exploring MR-TADF molecules as the lasing gain medium remains limited. Thus, a deeper understanding of the structure-property relationships governing their laser performance is highly required.

MR-TADF molecules typically exhibit localized frontier molecular orbitals, contributing to narrow emission spectra and high color purity. Undoubtedly, modifying the MR molecular skeleton, such as incorporating or fusing electron-donating/withdrawing substituents, can disrupt frontier molecular orbital distributions, thereby diminishing MR characteristics.[36] For instance, extending π–conjugation in the MR framework can shift the wavefunction away from the MR core, leading to an undesired charge-transfer state and reducing oscillator strengths.[37,38] Moreover, MR-TADF molecules have a strong tendency to aggregate in the solid state, causing concentration quenching and reduced emission efficiency,[39] which are detrimental to realizing lasing properties.[40] Recent molecular design strategies, including the incorporation of bulky peripheral substituents or the introduction of twisted structures, have been explored to prevent close packing and preserve emissive properties in OLEDs.[41] However, their intrinsic molecular aggregation nature at the low doping concentration (like 1 wt%), and their impact on organic lasing performance have not been extensively discussed. Additionally, the excited-state dynamics of MR dyes, particularly ESA, which is often overlooked but plays a critical role in lasing performance, are highly sensitive to modification of the MR skeleton. Unfortunately, the insufficient comprehension of ESA and triplet contribution in MR-TADF systems remains a significant obstacle to the advancement of organic laser development.

In this study, starting from a 9-(phenylcarbazol-3-yl)-9H-carbazole-3-carbonitrile (CzBN) core, we investigate the lasing performance of three MR-TADF derivatives. These derivatives featuring peripheral substituents of *t*-Bu and Ph groups were chosen to evaluate varying degrees of steric hindrance and electronic effects. Both substituent groups could enhance the oscillator strength without significantly altering the electronic properties of the emissive core. Therefore, two CzBN derivatives exhibited faster radiative decay rates ($k_r \sim 1.6–2.0 \times 10^8$ s^{-1}) in a solution state. However, the photophysical properties diverge significantly in the solid state across doping concentrations ranging from 0.6 wt% to 6 wt%. Notably, CzBN-tBu at 1 wt% doping in 3,3′-di(9H-carbazol-9-yl)-1,1′-biphenyl (mCBP) matrix, demonstrated superior ASE and lasing performance, achieving an optimal distributed feedback (DFB) lasing threshold of 3.4 μJ cm^{-2}. In contrast, despite its larger oscillator strength, CzBN-Ph with Ph substituents, exhibits a much higher lasing threshold of 15.1 μJ cm^{-2} at the same doping concentration. Given that low doping is generally believed to prevent aggregation, this unexpected behavior is attributed to the inherent molecular aggregation nature of MR molecules, even at low doping levels. Furthermore, *t*-Bu substitution preserved the separation of ESA spectra from the stimulated emission region. In contrast, Ph modification extends the ESA band, leading to a substantial overlap with the ASE and lasing spectra. By systematically investigating the lasing behavior of these CzBN-based emitters with varying peripheral substituents, this study elucidates the crucial role of peripheral modifications in modulating the molecular interaction and ESA characteristic, thus, optimizing the stimulated emission process.

Results and Discussion

Molecular Design and Photophysical Properties

To investigate the distributions of frontier molecular orbitals, density functional theory (DFT) and time-dependent DFT (TD-DFT) calculations using the *B3LYP/6–31*** method were performed. The molecular structures of CzBN derivatives, modified with *t*-Bu and Ph groups, are illustrated in Figure 1a–c. Here, the lowest unoccupied molecular orbitals (LUMOs) are primarily localized on the boron atom and the carbon atoms at its ortho positions, while the highest occupied molecular orbitals (HOMOs) are on the nitrogen atoms and at the *meta*-position of a central boron atom. The *t*-Bu substituents at the peripheral positions of the CzBN skeleton are barely involved in the electronic wavefunction distribution. As shown in Figure 1b, the slight extension of HOMO at *t*-Bu groups enhances the MR effect by strengthening the electron-donating ability of nitrogen atoms, thus, increasing its oscillator strength for the $S_0 \rightarrow S_1$ transition ($f = 0.410$) than that of CzBN ($f = 0.343$).[42–44] In comparison, the HOMO of CzBN-Ph significantly extends to the peripheral Ph groups through the reinforced π–conjugation.[45] This π–conjugation extension in CzBN-Ph results in a narrower energy bandgap, as well as much enhanced oscillator strength ($f = 0.522$), suggesting an expected higher radiative decay rate compared to the pristine CzBN core.

Photophysical measurements in dilute toluene solution (Figure 1d–f) reveal intrinsically narrow emission spectra of MR-TADF emitters. The ultraviolet/visible (UV-Vis) absorption and photoluminescence (PL) spectra of the three compounds align well with the redshift trend in previous reports.[37–40] The PL emission maxima are observed at 476 nm (CzBN), 484 nm (CzBN-tBu), and 495 nm (CzBN-Ph), respectively. The emission redshift in CzBN-tBu and CzBN-Ph can be ascribed to a reduced energy bandgap. All emitters show a very limited Stokes shift and the narrow full width at half maxima (FWHM) of 26 nm, 25 nm, and 24 nm for CzBN, CzBN-tBu, and CzBN-Ph, indicating that neither *t*-Bu nor Ph substituents impact the rigidity of molecular skeleton. As predicted by theoretical calculation, the larger

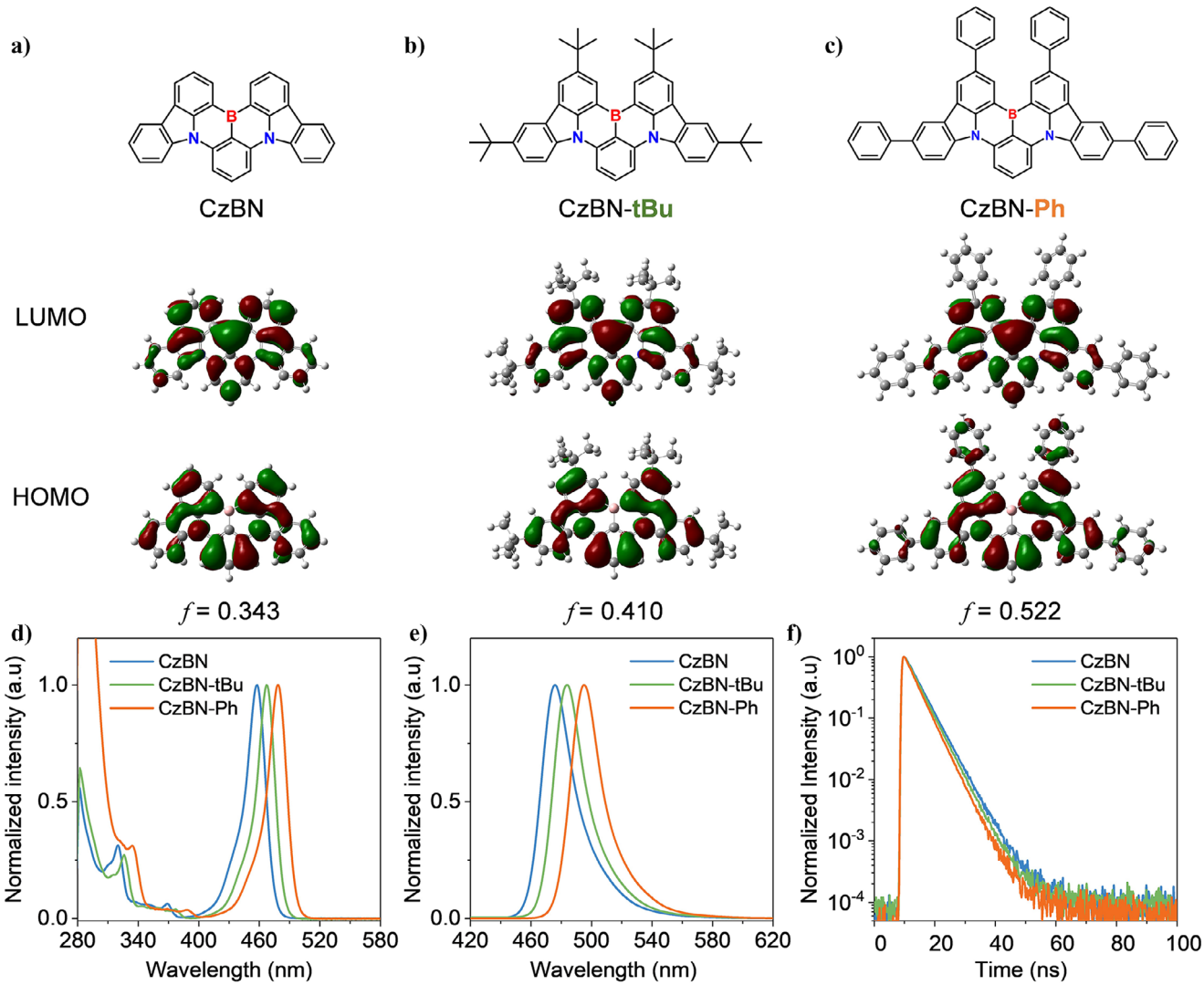

Figure 1. Molecular structures and frontier molecular orbital (LUMO/HOMO) distributions of a) CzBN, b) CzBN-tBu, and c) CzBN–Ph. Photophysical properties: d) Ultraviolet/visible (UV/Vis) absorption, e) PL spectra at room temperature (298K), and f) time-resolved PL spectra of CzBN derivatives in dilute toluene solution (10^{-5} mol L^{-1}) at room temperature (298K).

Table 1: Summary of photophysical properties of CzBN, CzBN-tBu, and CzBN-Ph.

Material	λ_{abs} [a] (nm)	λ_{em} [a),c] (nm)	ΔE_{ST} [a]	FWHM [a),c] (nm)	Φ [a),b),c] (%)	τ_P [a] (ns)	k_r [a] (10^8 s^{-1})	k_{RISC} [c] (10^4 s^{-1})	E_{th} (μJ cm^{-2})	λ_{ASE} (nm)
CzBN	458	476/484	0.15	25.5/33.4	74/100/83	4.7	1.6	0.91	16.3	495
CzBN-tBu	467	484/490	0.16	24.7/28.3	84/100/80	4.4	1.9	0.60	11.4	505
CzBN-Ph	479	495/503	0.13	24.3/36.2	83/100/73	4.1	2.0	0.95	22.6	512

[a] Measured in dilute toluene solution at room temperature (298 K). [b] Measured in dilute toluene solution after bubbling with nitrogen (10^{-5} mol L^{-1}). [c] Measured in mCBP host with 1 wt% doping concentration under Argon.

oscillator strengths for the $S_0 \rightarrow S_1$ transition of CzBN-tBu and CzBN-Ph lead to a shorter transient decay lifetime (Figure 1f) and faster radiative rate ($k_r \sim 2.0 \times 10^8$ s^{-1}). Therefore, CzBN-tBu and CzBN-Ph have the potential for enhanced lasing activity. The photophysical properties are summarized in Table 1. The singlet-triplet splitting energies for CzBN, CzBN-tBu, and CzBN-Ph are measured to be 0.15 , 0.16 , and 0.13 eV, respectively from low temperature (77 K) measurements in Figure S1. The results align well with the tendency of the simulated values (0.20 , 0.22 , and 0.19 eV) from the higher-level calculation results (Quantum chemical calculation section in Supplementary Information, Figure S2). Meanwhile, with the involvement of sufficient $T_2 \rightarrow S_1$ transition, CzBN-Ph exhibits a larger RISC rate (0.95×10^4 s^{-1}) than that of CzBN-tBu (0.60×10^4 s^{-1}) due to a larger spin-orbital coupling (Figure S3 and Table 1).

As another characteristic typical of MR-TADF molecules, the intrinsic planarity of the CzBN core is prone to induce

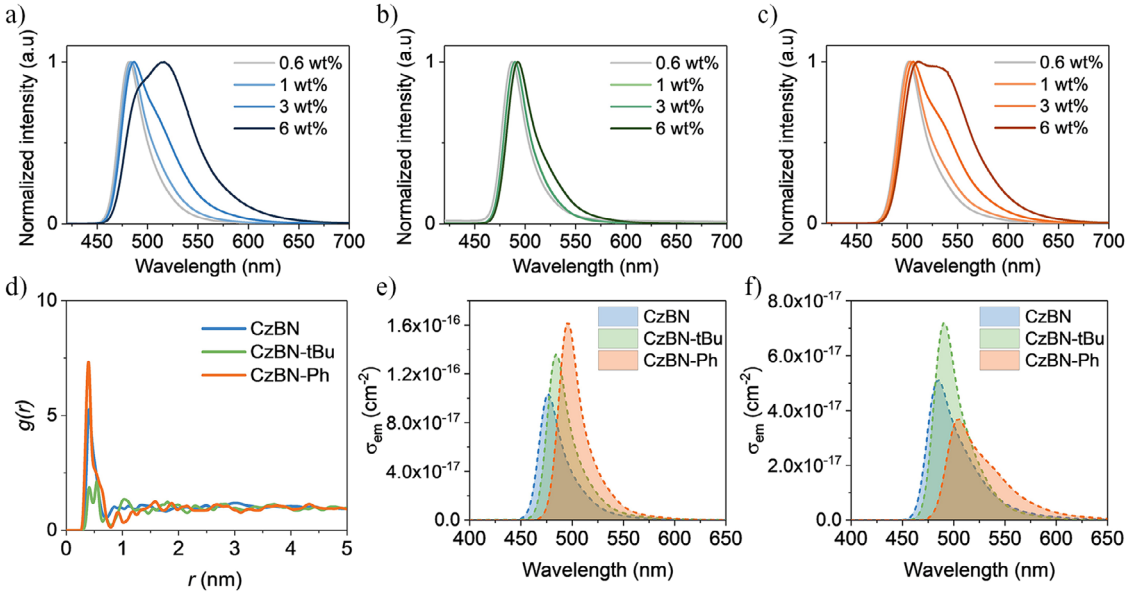

Figure 2. a) PL spectral evolution as doping concentration increases from 0.6 wt% to 6 wt% for a) CzBN, b) CzBN-tBu, and c) CzBN-Ph in mCBP host. d) RDF g(r) of emitters at 6 wt% doping concentration. The stimulated emission cross-section coefficient e) in solution phase (toluene, 10^{-5} mol L^{-1}) and f) in mCBP host at 1 wt% doping concentration.

molecule aggregation in the solid-state films, resulting in detrimental effects, like the formation of excimer and exciton quenching. To further investigate the photophysical properties in the solid-state films, mCBP is used as the host matrix, where the emitters are doped at different concentrations of 0.6, 1, 3, and 6 wt% (Table S1). As illustrated in Figure 2a, the emission FWHMs of CzBN-based blend films expand from 30.3 to 71.9 nm, accompanied by a noticeable redshift in the emission maximum from 482 to 516 nm. Similarly, CzBN-Ph exhibited the identical trend of the FWHM broadening and redshifted emission, suggesting that the peripheral Ph substituent fails to suppress the molecular aggregation (Figure 2c). Due to the prolonged decay lifetime from the excimers, their corresponding k_r values substantially decreased to around $0.25 \times 10^8\ s^{-1}$. In contrast, CzBN-tBu, with its nonconjugated extension, maintains stable FWHM values (from 27.6 to 32.9 nm) and localized emission wavelengths (from 488 to 493 nm). Notably, at a 6 wt% doping concentration, its blend film exhibits a k_r of around $0.8 \times 10^8\ s^{-1}$, implying the steric hindrance of *t*-Bu motifs effectively mitigates both aggregation-induced quenching and excimer formation (Table S1). Furthermore, it ought to be highlighted that the molecular aggregation in CzBN and CzBN-Ph is prone to occur even at a low doping concentration of 1 wt%. As illustrated in Figure S4a,b, the FWHM differences of CzBN, CzBN-tBu, and CzBN-Ph between the dilute solution and 1 wt% blend films are 35, 14, and 52 meV, respectively, which indicates more severe molecular aggregation for CzBN and CzBN-Ph. Moreover, comparing the single-exponential decay characteristic in toluene, both CzBN and CzBN-Ph display multiple-exponential decay with longer radiative lifetime (Table S1), suggesting the presence of intermolecular interactions. Additionally, as depicted in Figure S5, when increasing the doping concentration up to 6 wt%, the deviation of the transient decay curve becomes more pronounced, indicating the enhanced excimer emission, which aligns with the spectral change in Figure 2a–c. Conversely, CzBN-tBu-based blend films retain their spectral profile and exhibit single-exponential decay at both 1 and 6 wt% doping concentrations, effectively preventing the excimer formation. Notably, comparing the typical light-emitting applications, like OLEDs, organic lasing dyes exhibit a heightened sensitivity to molecular packing alignments and excited-state dynamics. Consequently, further investigation into the molecular dynamics of three CzBN derivatives is warranted.

Molecular Dynamics Simulation

To elucidate the working mechanism of three different guest molecules, we conducted all-atom molecular dynamics (AA-MD) simulations on three distinct MR-TADF systems. Detailed methodological protocols are documented in the "Molecular Dynamics Simulations" section in the experimental section in Supplementary Information. Through analysis of the radial distribution function (RDF) g(r) parameter, which quantifies the spatial probability distribution between molecules, we investigated aggregation tendencies among the emitters. We note that the RDFs measure the probability of finding a particle some distance away from a reference particle, with a higher g(r) peak pointing to a larger packing density at a given distance. As shown in Figure 2d, the CzBN and CzBN-Ph system demonstrated the most significant aggregation propensity at the 6 wt% doping concentration, evidenced by a prominent RDF peak centered within the 0.5 nm intermolecular distance range. This dense molecular packing likely facilitates excitonic interactions through π-π overlap, thereby promoting nonradiative decay pathways

and consequently reducing the effective k_r. In contrast, the CzBN-tBu system exhibited substantially suppressed aggregation characteristics relative to CzBN-Ph. This notable improvement in the molecular dispersion can be attributed to impeding π–π stacking interactions of the steric hindrance of peripheral *t*-Bu substituents. In terms of 1 wt% doping concentration, MD simulations in Figure S6 indicate that both CzBN-Ph and CzBN molecules in the 1 wt% blend film exhibit face-to-face stacking, with shorter centroid distances. In contrast, CzBN-tBu molecules in the blend film demonstrate a longer distance, effectively reducing the possibility of π-π stacking. These simulation results are well-aligned with our experimental observations.

Furthermore, we examined the stimulated emission coefficient (σ_{em}), which influences the efficiency of the lasing process. σ_{em} is calculated by Equation 1:

$$\sigma_{em}(\lambda) = \frac{\lambda^4 E_f(\lambda)}{8\pi n^2(\lambda) c \tau_f} \quad (1)$$

where $E_f(\lambda)$ represents the distribution of PLQY over wavelength, n(λ) denotes the refractive index of the active layer, and τ_f is the fluorescence lifetime.[30] σ_{em} is primarily affected by the radiative decay rate. CzBN-Ph exhibits the highest value of 7.2×10^{-17} cm^{-2} in the solution state, followed by CzBN-tBu and CzBN (Figure 2e). In contrast, CzBN-tBu shows the highest value of 4.5×10^{-17} cm^{-2} in the blend film, followed by CzBN and CzBN-Ph at their respective ASE wavelengths (Figure 2f). This discrepancy between solution and film states is due to molecular aggregation.

Performance of ASE

To assess the lasing activity of three emitters, ASE measurements were conducted with three emitters at the doping concentrations of 1, 3, and 6 wt% in the mCBP host. The mCBP was chosen as a host due to its high singlet and triplet energy levels, ensuring efficient energy transfer (Figure S7), and the high PLQY of the emitters (Figure S8 and Table S2). Films with 100 nm thickness were deposited on a quartz substrate to ensure sufficient waveguiding and were then excited using a stripe-shaped excitation beam, and edge-emitted light was measured with an increase in excitation power. All three emitters successfully showed ASE behaviors, as shown in Figure 3a–c and Table S1. The ASE thresholds were derived from the intersection of linear fits to the linear and nonlinear regions of the emission intensity as a function of the excitation intensity plot. The FWHM of the emitters at low excitation fluences are broad, but as the excitation pump fluence increases, the narrow emission emerges (Figure S9). At high excitation pump fluences, the ASE spectra exhibited FWHMs less than 8 nm (Figure 3d–f). Additionally, the CzBN derivatives demonstrated enhanced ASE stability compared to their parent skeleton, DABNA-1, due to their fused and rigid core structures (Figure S10).[35]

Generally, the tendency of the ASE performance is inversely proportional to the doping concentrations. Specifically, the ASE thresholds for CzBN-based blend films significantly increased from 16.3 to 54.2 μJ cm^{-2} as the doping concentrations rose (Figure 3a). In the case of CzBN-Ph, the ASE activity disappeared at 6 wt%, demonstrating that severe molecular aggregation disrupts the population inversion process (Figure 3c). In comparison, CzBN-tBu-based blend films preserved robust ASE characteristics across all doping concentrations from 1 to 6 wt%, with ASE thresholds ranging from 8.2 to 13.2 μJ cm^{-2} (Figure 3b). At 1 wt% doping concentration, CzBN-tBu achieved the lowest ASE threshold of 11.4 μJ cm^{-2} at 505 nm, which is lower than those of the pristine CzBN (16.3 μJ cm^{-2}) and CzBN-Ph (22.6 μJ cm^{-2}). It ought to be noted that the ASE thresholds fail to align with their oscillator strength (Figure S11). For instance, although CzBN-Ph also possesses a larger oscillator strength than CzBN and CzBN-tBu, its ASE threshold remains elevated. This unexpected result can be partially ascribed to the overlooked molecular aggregation at 1 wt% doping concentration. On the other hand, CzBN-tBu exhibits the lowest ASE threshold across 0.6 to 6 wt% doping concentrations. However, the threshold began to increase once the doping concentration reached 6 wt%, indicating the limitation of the *t*-Bu group in further preventing aggregate formation. Besides an inherent aggregation propensity from a longer π–conjugation skeleton (Figure 2a), the characteristics of their excited-state dynamics are also critical. Therefore, the picosecond-scale transient ESA was conducted.

The singlet ESA spectra were measured in toluene (Figure 3g–i). There is a negligible overlap between the ESA bands and the ASE spectra of CzBN and CzBN-tBu. As shown in Figure 3h, introducing the *t*-Bu group caused no significant change in the ESA band. In contrast, adding the Ph group induced a noticeable blueshift in the ESA band. This, combined with the redshift in emission due to increased π–conjugation, led to a more significant overlap with the resulting ASE spectra. Consequently, the different peripheral substituents of *t*-Bu and Ph result in different excited-state behaviors. This observation also could partially explain why ASE was still observed in the 6 wt% doped CzBN film but was challenging to achieve in the 6 wt% doped CzBN-Ph film, despite both experiencing significant aggregation.

DFB Lasing

To obtain the lasing emission, we employed a DFB resonator commonly used for organic thin-film lasers. Surface-emitting DFB lasers utilize a grating structure with an appropriate period selected for the second-order operation. The DFB of the oscillating guided modes is provided through the second-order Bragg scattering induced by substrate corrugations. These modes are coupled to radiation in a direction perpendicular to the substrate plane via first-order scattering. Laser oscillation occurs near the Bragg resonance wavelength, which is described by the following Equation 2:

$$m\lambda_{Bragg} = 2n_{eff}\Lambda_m \quad (2)$$

where m is the diffraction order, λ_{Bragg} is the Bragg wavelength, n_{eff} is the effective refractive index of the gain

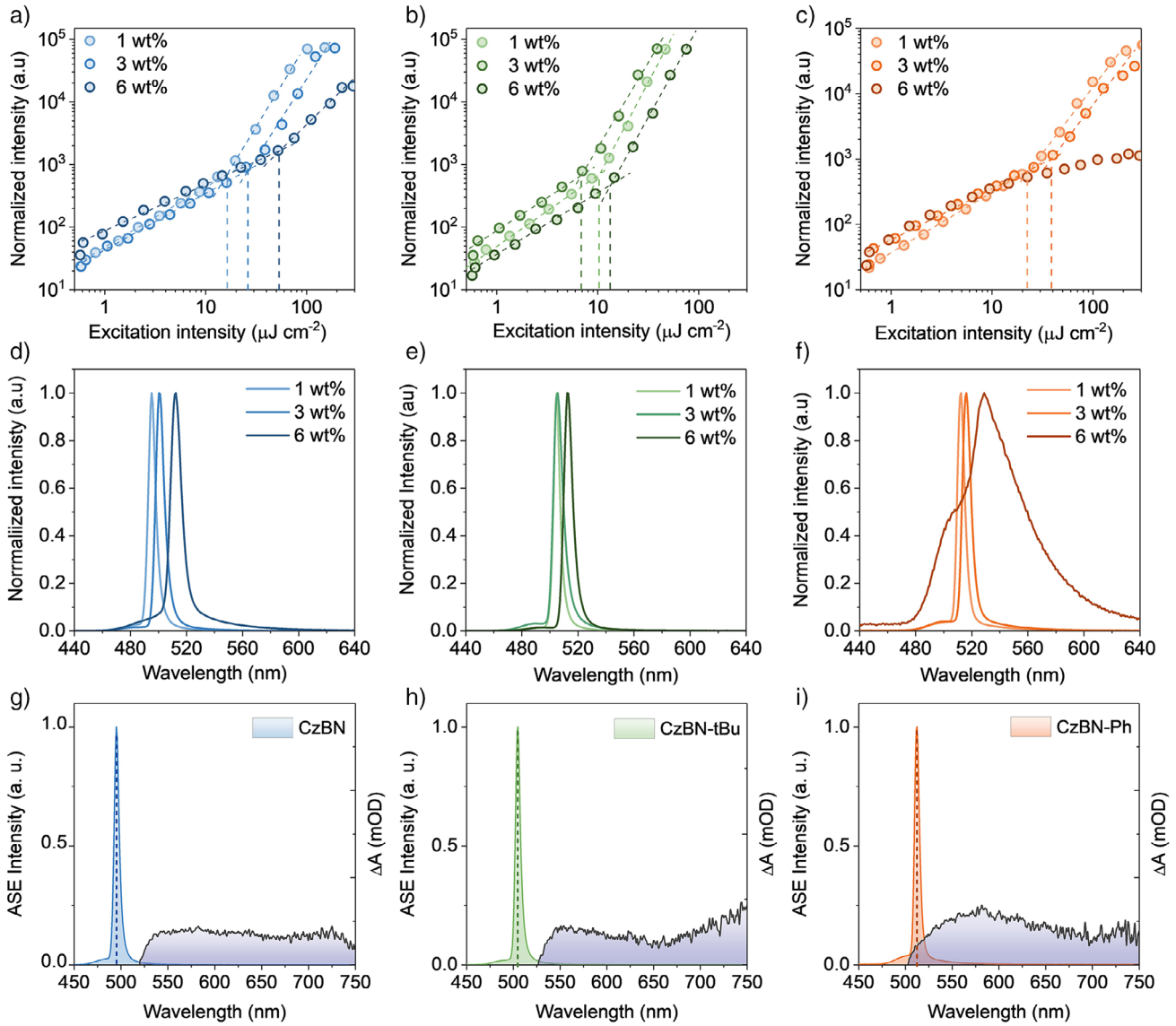

Figure 3. Input-output intensity characteristic plots of emission intensity and emission line width as a function of excitation intensity of a) CzBN, b) CzBN-tBu, and c) CzBN-Ph at 1 wt% in mCBP film. The corresponding ASE spectra of emitters d) CzBN, e) CzBN-tBu, and f) CzBN-Ph at the above threshold condition (~100 μJ cm^{-2}). Comparison of singlet absorption spectra (in toluene, 10^{-4} mol L^{-1}) and ASE spectra of g) CzBN, h) CzBN-tBu, and i) CzBN-Ph (1 wt% in mCBP).

medium, and Λ_m is the grating period.[31] In designing the DFB grating periods, the λ_{Bragg} was set to match the ASE peak wavelength of the emitters. The n_{eff} index is calculated to be around 1.55 with asymmetric waveguide geometry comprising an air ($n = 1.0$)/organic ($n = 1.7$)/SiO_2 ($n = 1.46$) structure.[46] The DFB grating pitch height is designed to be 70 nm. Subsequently, 1 wt% emitter: mCBP blend films with a thickness of 200 nm were vacuum-deposited onto the prepared DFBs (Figure S12). The input-output characteristic plots of the lasers from the three emitters are shown in Figure 4a.

As the excitation power increased, a noticeable change in the slope of emission intensity was observed, accompanied by a sharp decrease in the FWHM to less than 0.32 nm (Figures S13–S15), indicating the onset of laser emission. For CzBN, the laser emission emerged at 500 nm with a threshold energy of 5.5 μJ cm^{-2}, approximately three times lower than its ASE threshold. Meanwhile, CzBN-tBu exhibited the lowest threshold (3.4 μJ cm^{-2}) laser emission at 507.8 nm, highlighting its superior characteristics. In contrast, the CzBN-Ph laser showed laser emission at 519.4 nm with the highest threshold among all three emitters at (15.1 μJ cm^{-2}), consistent with the trend of ASE performance. Also, the lasing emissions appeared close to the ASE peak wavelengths as expected (Figure 4b). Furthermore, since the DFB resonator produces a strongly polarized single-mode laser beam, the degree of polarization (DOP) of the lasing emissions was calculated using the Equation 3:

$$DOP = (I_{||} - I_{\perp})/(I_{||} + I_{\perp}) \quad (3)$$

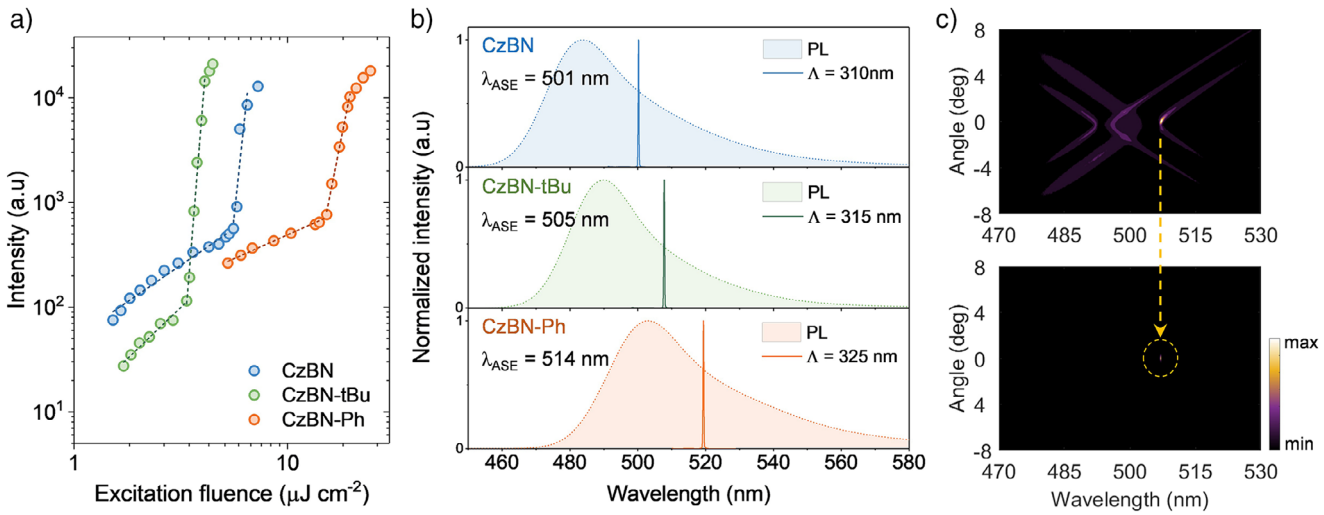

Figure 4. a) DFB lasing thresholds from input-output intensity characteristic plots of emission intensity and emission line width as a function of excitation intensity for CzBN, CzBNtBu, and CzBNPh. b) The lasing modes (line) and the corresponding PL spectra (shaded area). Angle-resolved PL spectra of 1 wt% CzBN-tBu: mCBP DFB laser at c) below (top) and above (bottom) threshold conditions (laser emission highlighted by the yellow arrow).

where $I_{\parallel}$ and $I_{\perp}$ are the intensity at 0° and 90° between the transmission axis of the polarizer and the grating direction, respectively.[35] The calculated DOP values were 0.99 for both CzBN and CzBN-tBu DFB devices, and 0.97 for the CzBN-Ph DFB device (Figure S16), indicating strong, linear transverse electric (TE) polarization characteristics. To further verify the lasing behavior, angle-resolved PL spectra of the CzBN-tBu DFB laser, which exhibited the lowest threshold, were recorded (Figure 4c). Below the lasing threshold, its waveguided emission is outcoupled by the DFB grating at various angles, resulting in the angle-dependent feature.[47] However, once the excitation laser power surpasses the lasing threshold, the monochromatic lasing emission (FWHM < 0.3 nm) emerges near 0°, providing direct evidence of the lasing process. These findings confirm the successful implementation and optimization of DFB lasers using our organic thin-film system. To further evaluate the contribution of TADF properties in MR lasing dyes, temperature-dependent measurements are conducted to systematically investigate the DFB lasing performance of the 1 wt% CzBN-tBu: mCBP film.[24] The temperature was gradually decreased from room temperature (295K) to 220K in steps. As shown in Figures S17 and S18, the DFB lasing threshold increased from 8.0 to 29.2 μJ cm^{-2} as the temperature dropped to 240K. Upon further cooling to 220K, the lasing threshold of CzBN-tBu rose significantly to 201 μJ cm^{-2}. Notably, when the temperature was restored to room temperature (295K), the lasing threshold decreased back to approximately 10 μJ cm^{-2}. This trend of increasing lasing thresholds with decreasing temperature is unconventional compared to typical fluorescent lasing dyes.[48] For direct comparison, we measured the temperature-dependent lasing threshold of the fluorescent dye BSBCz-EH under identical conditions (Figure S19). Unlike CzBN-tBu, the BSBCz-EH-based blend film maintained a stable lasing threshold of around 3 μJ cm^{-2} with no significant variation across the temperature range. Therefore, the distinct temperature-dependent lasing behavior observed in CzBN-tBu partially suggests the possible contribution of up-converted triplets in MR-TADF lasing dyes, reinforcing the potential of MR-TADF molecules in lasing applications.

Conclusion

This study highlights the crucial role of peripheral modifications in shaping the molecular packing, photophysical properties, ASE behavior, and lasing performance of CzBN derivatives. Although both *t*-Bu and Ph substituents enhance oscillator strength, improving photophysical properties in solution, their effects in the solid state differ significantly even under low doping ratios. CzBN-Ph with conjugation extension promotes undesirable molecular aggregation and increases spectral overlap between the ESA band and the ASE region, ultimately limiting its lasing potential. In contrast, *t*-Bu groups effectively suppress aggregation through steric hindrance while maintaining a separation between the ESA and ASE regions. This leads to a lower ASE threshold and the retention of favorable photophysical properties across a wide range of doping concentrations. These findings underscore the importance of rational peripheral modification, not only in mitigating molecular aggregation and tuning lasing wavelengths via frontier molecular orbital engineering but also in optimizing excited-state properties. This strategic approach is pivotal for advancing MR-TADF emitters, paving the way for sufficient triplet harvesting for lasing and the development of electrically driven TADF laser devices in the future.

Acknowledgements

We thank Dr. Buddhika S. B. Karunathilaka, Nobuhiro Takeishi, and Keiko Kusuhara for their technical assistance.

This work was supported by the Japan Science and Technology Agency (JST) CREST (grant no. JPMJCR22B3), Japan Society for the Promotion of Science (JSPS) Specially Promoted Research (grant no. 23H05406), and International Leading Research (ILR) (grant no. 23K20039), the Ministry of Education, Culture, Sports, Science and Technology (MEXT), Japan. X.T. acknowledges the financial support from JSPS KAKENHI (grant no. 22K20536). X.-K.C. acknowledges the financial support from the National Natural Science Foundation of China (grant no. 52473190), the Natural Science Foundation of Jiangsu Province (grant no. BK20240042), the Science and Technology Project of Suzhou (grant no. ZXL2024394), Suzhou Key Laboratory of Functional Nano and Soft Materials, Collaborative Innovation Center of Suzhou Nano Science and Technology, and the 111 Project.

Conflict of Interests

The authors declare no conflict of interest.

Data Availability Statement

The data that support the findings of this study are available from the corresponding author upon reasonable request.

Keywords: Excited State Absorption · Molecular Aggregation · Multiple Resonance · Organic Lasers · Peripheral Substituents

[1] T. H. Maiman, *Nature* **1960**, *187*, 493–494.
[2] P. P. Sorokin, J. R. Lankard, *IBM J. Res. Dev.* **1966**, *10*, 162–163.
[3] F. P. Schäfer, W. Schmidt, J. Volze, *Appl. Phys. Lett.* **1966**, *9*, 306–309.
[4] I. D. W. Samuel, G. A. Turnbull, *Chem. Rev.* **2007**, *107*, 1272–1295.
[5] A. J. C. Kuehne, M. C. Gather, *Chem. Rev.* **2016**, *116*, 12823–12864.
[6] K. Yoshida, J. Gong, A. L. Kanibolotsky, P. J. Skabara, G. A. Turnbull, I. D. W. Samuel, *Nature* **2023**, *621*, 746–752.
[7] F. Strieth-Kalthoff, H. Hao, V. Rathore, J. Derasp, T. Gaudin, N. H. Angello, M. Seifrid, E. Trushina, M. Guy, J. Liu, X. Tang, M. Mamada, W. Wang, T. Tsagaantsooj, C. Lavigne, R. Pollice, T. C. Wu, K. Hotta, L. Bodo, S. Li, M. Haddadnia, A. Wołos, R. Roszak, C. T. Ser, C. Bozal-Ginesta, R. J. Hickman, J. Vestfrid, A. Aguilar-Granda, E. L. Klimareva, R. C. Sigerson, et al., *Science* **2024**, *384*, eadk9227.
[8] M. Lehnhardt, T. Riedl, T. Weimann, W. Kowalsky, *Phys. Rev. B – Condens. Matter Mater. Phys.* **2010**, *81*, 1–5.
[9] S. Chénais, S. Forget, *Polym. Int.* **2012**, *61*, 390–406.
[10] A. S. D. Sandanayaka, T. Matsushima, F. Bencheikh, S. Terakawa, W. J. Potscavage, C. Qin, T. Fujihara, K. Goushi, J. C. Ribierre, C. Adachi, *Appl. Phys. Express* **2019**, *12*, 061010.
[11] C. Adachi, A. S. D. Sandanayaka, *CCS Chem.* **2020**, *2*, 1203–1216.
[12] M. Inoue, T. Matsushima, C. Adachi, *Appl. Phys. Lett.* **2016**, *108*, 133302.
[13] A. Shukla, M. Hasan, G. Banappanavar, V. Ahmad, J. Sobus, E. G. Moore, D. Kabra, S.-C. Lo, E. B. Namdas, *Commun. Mater.* **2022**, *3*, 27.
[14] Y. Oyama, M. Mamada, A. Shukla, E. G. Moore, S. C. Lo, E. B. Namdas, C. Adachi, *ACS Mater. Lett.* **2020**, *2*, 161–167.
[15] B. S. B. Karunathilaka, U. Balijapalli, C. A. M. Senevirathne, Y. Esaki, K. Goushi, T. Matsushima, A. S. D. D. Sandanayaka, C. Adachi, *Adv. Funct. Mater.* **2020**, *30*, 2001078.
[16] X. Tang, U. Balijapalli, D. Okada, B. S. B. Karunathilaka, C. A. M. Senevirathne, Y. Lee, Z. Feng, A. S. D. Sandanayaka, T. Matsushima, C. Adachi, *Adv. Funct. Mater.* **2021**, *31*, 2104529.
[17] C. A. M. Senevirathne, S. Yoshida, M. Auffray, M. Yahiro, B. S. B. Karunathilaka, F. Bencheikh, K. Goushi, A. S. D. Sandanayaka, T. Matsushima, C. Adachi, *Adv. Opt. Mater.* **2022**, *10*, 2101302.
[18] V. T. N. Mai, V. Ahmad, M. Mamada, T. Fukunaga, A. Shukla, J. Sobus, G. Krishnan, E. G. Moore, G. G. Andersson, C. Adachi, E. B. Namdas, S.-C. Lo, *Nat. Commun.* **2020**, *11*, 5623.
[19] H. Uoyama, K. Goushi, K. Shizu, H. Nomura, C. Adachi, *Nature* **2012**, *492*, 234–238.
[20] A. Endo, M. Ogasawara, A. Takahashi, D. Yokoyama, Y. Kato, C. Adachi, *Adv. Mater.* **2009**, *21*, 4802–4806.
[21] D. H. Kim, A. D'Aléo, X. K. Chen, A. D. S. Sandanayaka, D. Yao, L. Zhao, T. Komino, E. Zaborova, G. Canard, Y. Tsuchiya, E. Choi, J. W. Wu, F. Fages, J. L. Brédas, J. C. Ribierre, C. Adachi, *Nat. Photonics* **2018**, *12*, 98–104.
[22] Z. Zhou, C. Qiao, K. Wang, L. Wang, J. Liang, Q. Peng, Z. Wei, H. Dong, C. Zhang, Z. Shuai, Y. Yan, Y. S. Zhao, *Angew. Chem. Int. Ed.* **2020**, *59*, 21677–21682.
[23] Y. Li, K. Wang, Q. Liao, L. Fu, C. Gu, Z. Yu, H. Fu, *Nano Lett.* **2021**, *21*, 3287–3294.
[24] T. Zhang, Z. Zhou, X. Liu, K. Wang, Y. Fan, C. Zhang, J. Yao, Y. Yan, Y. S. Zhao, *J. Am. Chem. Soc.* **2021**, *143*, 20249–20255.
[25] A. Abe, K. Goushi, A. S. D. Sandanayaka, R. Komatsu, T. Fujihara, M. Mamada, C. Adachi, *J. Phys. Chem. Lett.* **2022**, *13*, 1323–1329.
[26] D. Chen, J. Gong, J. Grüne, T. Matulaitis, A. J. Gillett, X. Zhang, I. D. W. Samuel, G. A. Turnbull, E. Zysman-Colman, *Adv. Funct. Mater.* **2024**, *34*, 2409592.
[27] A. Shukla, S. K. M. McGregor, R. Wawrzinek, S. Saggar, E. G. Moore, S. Lo, E. B. Namdas, *Adv. Funct. Mater.* **2021**, *31*, 2009817.
[28] T. Hatakeyama, K. Shiren, K. Nakajima, S. Nomura, S. Nakatsuka, K. Kinoshita, J. Ni, Y. Ono, T. Ikuta, *Adv. Mater.* **2016**, *28*, 2777–2781.
[29] S. M. Suresh, D. Hall, D. Beljonne, Y. Olivier, E. Zysman-Colman, *Adv. Funct. Mater.* **2020**, *30*, 1908677.
[30] H. Nakanotani, T. Furukawa, T. Hosokai, T. Hatakeyama, C. Adachi, *Adv. Opt. Mater.* **2017**, *5*, 1700051.
[31] M. Mamada, S. Maedera, S. Oda, T. B. Nguyen, H. Nakanotani, T. Hatakeyama, C. Adachi, *Mater. Chem. Front.* **2022**, *7*, 259–266.
[32] H. Jiang, J. Jin, W. Wong, *Adv. Funct. Mater.* **2023**, *33*, 2306880.
[33] G. Meng, H. Dai, Q. Wang, J. Zhou, T. Fan, X. Zeng, X. Wang, Y. Zhang, D. Yang, D. Ma, D. Zhang, L. Duan, *Nat. Commun.* **2023**, *14*, 2394.
[34] Y. Yu, S. Mallick, M. Wang, K. Börjesson, *Nat. Commun.* **2021**, *12*, 3255.
[35] X. Tang, M. Xie, Z. Lin, K. Mitrofanov, T. Tsagaantsooj, Y. Lee, R. Kabe, A. S. D. Sandanayaka, T. Matsushima, T. Hatakeyama, C. Adachi, *Angew. Chem. Int. Ed.* **2024**, *63*, e202315210.
[36] H. S. Kim, H. J. Cheon, D. Lee, W. Lee, J. Kim, Y.-H. Kim, S. Yoo, *Sci. Adv.* **2023**, *9*, eadf1388.
[37] M. Yang, S. Shikita, H. Min, I. S. Park, H. Shibata, N. Amanokura, T. Yasuda, *Angew. Chem. Int. Ed.* **2021**, *60*, 23142–23147.

[38] J. M. dos Santos, C.-Y. Chan, S. Tang, D. Hall, T. Matulaitis, D. B. Cordes, A. M. Z. Slawin, Y. Tsuchiya, L. Edman, C. Adachi, Y. Olivier, E. Zysman-Colman, *J. Mater. Chem. C* **2023**, *11*, 8263–8273.
[39] L. Xiaofeng, Z. Dongdong, D. Lian, Z. Yuewei, *Front. Chem.* **2023**, *11*, 1198404.
[40] C. C. Yan, X. D. Wang, L. S. Liao, *Adv. Sci.* **2022**, *9*, 1–10.
[41] R. Braveenth, K. Raagulan, Y.-J. Kim, B.-M. Kim, *Mater. Adv.* **2023**, *4*, 374–388.
[42] S. Xu, Q. Yang, Y. Zhang, H. Li, Q. Xue, G. Xie, M. Gu, J. Jin, L. Huang, R. Chen, *Chinese Chem. Lett.* **2021**, *32*, 1372–1376.
[43] Y. Lee, C. Chan, M. Tanaka, M. Mamada, U. Balijapalli, Y. Tsuchiya, H. Nakanotani, T. Hatakeyama, C. Adachi, *Adv. Electron. Mater.* **2021**, *7*, 2001090.
[44] S. Wang, Y. Xu, J. Miao, T. Hua, X. Cao, N. Li, Z. Huang, C. Yang, *Chem. Eng. J.* **2023**, *471*, 144664.
[45] Y. Xu, Z. Cheng, Z. Li, B. Liang, J. Wang, J. Wei, Z. Zhang, Y. Wang, *Adv. Opt. Mater.* **2020**, *8*, 1902142.
[46] M. Hammer, 1-D Mode Solver for Dielectric Multilayer Slab Waveguides, https://www.computational-photonics.eu/oms.html.
[47] G. A. Turnbull, P. Andrew, M. J. Jory, W. L. Barnes, I. D. W. Samuel, *Phys. Rev. B* **2001**, *64*, 125122.
[48] V. G. Kozlov, V. Bulović, S. R. Forrest, *Appl. Phys. Lett.* **1997**, *71*, 2575–2577.

Manuscript received: February 26, 2025
Revised manuscript received: March 24, 2025
Accepted manuscript online: March 28, 2025
Version of record online: April 07, 2025